PERGAMON

International Journal of Heat and Mass Transfer 42 (1999) 3803–3814

International Journal of HEAT and MASS TRANSFER

www.elsevier.com/locate/ijhmt

Effect of cross-sectional aspect ratio on turbulent heat transfer in an orthogonally rotating rectangular smooth duct

Akira Murata[a,*], Sadanari Mochizuki[b]

[a]Graduate School of Bio-Applications and Systems Engineering, Tokyo University of Agriculture & Technology, 2-24-16 Nakacho, Koganei, Tokyo 184-8588, Japan

[b]Department of Mechanical Systems Engineering, College of Engineering, Tokyo University of Agriculture and Technology, 2-24-16 Nakacho, Koganei, Tokyo 184-8588, Japan

Received 14 July 1998; received in revised form 12 January 1999

Abstract

In order to investigate the effects of the Coriolis force and the duct cross-sectional aspect ratio on turbulent heat transfer, the large eddy simulation was performed changing the aspect ratio and the rotation number in the range, 0.25–4.0 and 0–5.0, respectively, while the turbulent Reynolds number was 350. In the results, both direct and indirect influences of the Coriolis force on the turbulence were seen. The relative intensity of these influences depended on the aspect ratio. The Colburn's j factor showed a higher value for a larger aspect ratio because of larger heat transfer enhancement on the pressure and side surfaces.

1. Introduction

In the development of high performance gas turbines, effective blade cooling is essential because the higher efficiency of the turbine requires a higher inlet gas temperature. Generally, this blade cooling is performed by film cooling at the external surface of the turbine blade and also by internal forced-convection cooling which uses winding flow passages inside the turbine blade. In internal forced-convection cooling, the real phenomena are made very complicated by external forces: the Coriolis force and the buoyancy force in the centrifugal acceleration field. In addition to these external forces, the effects induced by a 180° sharp turn and turbulence promoters (ribs) installed on the internal surface result in phenomena that are far from understood [1].

Many researchers have investigated internal forced-convective cooling experimentally [2]. On the other hand, in previous numerical studies, for even a straight smooth duct, most researchers adopted the Reynolds average Navier–Stokes equation with a turbulence model like the k–ϵ two equation model or the algebraic equation model [3]. Recent advancement in computers enables us to numerically simulate the fluctuating components of the turbulent flow by using the large eddy simulation (LES) or the direct numerical simulation (DNS). Because LES and DNS directly resolve temporal variation of the fluctuating components, the results are more universal, in other words, more free from the empirical modeling than the Reynolds average turbulence models. So far, the turbulent flow in a stationary square duct was solved using DNS [4,5] and LES [6,7]. As Launder et al. [8] pointed out, it should

* Corresponding author.

0017-9310/99/$ - see front matter
PII: S0017-9310(99)00058-7

Nomenclature

A_R	duct cross-sectional aspect ratio ($=H/W$)
c_p	specific heat
C_f	friction coefficient ($=\tau_w/(0.5\rho U_m^2)$)
C_S	Smagorinsky constant
D	hydraulic diameter ($=2HW/(H+W)$)
F_i	external force term
h	heat transfer coefficient
H	duct height
j	Colburn's j factor ($=Nu_m/(Re_m Pr^{1/3})$)
k	turbulent kinetic energy
l	length scale ($=0.5D$)
L_p	peripheral location
Nu	Nusselt number ($=hD/\lambda$)
Pr	Prandtl number ($=0.71$)
Pr_{SGS}	Prandtl number of subgrid-scale model ($=0.5$)
$\dot{q}$	wall heat flux
Re_m	Reynolds number ($=U_m D/\nu$)
Re_*	turbulent Reynolds number ($=u_* l/\nu$)
Ro_m	rotation number ($=\omega D/U_m$)
Ro_*	rotation number ($=\omega l/u_*$)
S_{ij}	rate-of-strain tensor
t	time
T	temperature
T_b	bulk temperature
T_r	friction temperature ($=\dot{q}/(\rho c_p u_*)$)
u, v, w	velocities in x, y, z directions
u_*	friction velocity
U_m	mean velocity
W	duct width
x, y, z	transverse, vertical, streamwise directions
$\Delta x, \Delta y, \Delta z$	grid spacing in x, y, z directions

Greek symbols

α_{SGSj}	subgrid-scale energy flux
λ	thermal conductivity
ν	kinematic viscosity
ν_t	subgrid-scale eddy viscosity
ω	angular velocity
ρ	density
θ	dimensionless temperature ($=(T-T_b)/T_r$)
τ_{SGSij}	subgrid-scale stress tensor
τ_w	wall shear stress

Subscripts and superscripts

B	Blasius
L	local value
m	duct average or based on mean velocity
w	wall
∞	fully developed
$*$	friction velocity
$+$	dimensionless value based on inner scales

be noted that in order to quantitatively simulate the flow in a rotating system, the second moment closure, that is, the Reynolds stress equation model, is a minimum requirement considering the non-isotropic effect of the Coriolis force on the turbulence.

The authors' group has performed heat transfer measurements of a square duct with smooth and rib-roughened surface configurations by using hundreds of thermocouples in rotating conditions [9] and a large eddy simulation of a smooth square straight duct with a dynamic subgrid-scale model in rotating conditions [10]. In the smooth straight duct results of these previous studies, the effects of the Coriolis force on peripheral variation of the local heat transfer coefficient, duct-averaged heat transfer, and friction coefficients were investigated. However, in real gas turbine blades, the cross-sectional aspect ratio of the cooling flow passage is not unity in most cases, and the effect of the cross-sectional aspect ratio on the heat transfer has not been investigated in the previous studies. Numerical results [11,12] are reported using the k–ϵ two equation turbulence model which showed that the aspect ratio changed the heat transfer due to the Coriolis induced secondary flow being strongly affected by the aspect ratio; therefore, further studies are necessary with a more elaborate treatment of turbulence such as LES or DNS.

This study deals with a fully developed turbulent flow and its heat transfer in a rectangular duct by using the large eddy simulation. The duct aspect ratio was varied in five different values ranging from 0.25 to 4.0. The effects of the Coriolis force and the aspect ratio on the heat transfer are focused on, and the relation between the local heat transfer and the flow structure is discussed.

2. Numerical analysis

Fig. 1 shows the computational domain and coordinate system used in this study. The duct has a rectangular cross section with a duct height of H and a duct width of W. The hydraulic diameter of the duct was calculated as $D=2HW/(H+W)$. The coordinate system was fixed to a rotating duct which had an angular velocity of ω. The streamwise (radially outward) direction was chosen in the z direction; the x and y directions were transverse and perpendicular directions to the trailing and leading walls, respectively. In this study, the duct cross-sectional aspect ratio, A_R $(=H/W)$, was varied among 0.25, 0.5, 1.0, 2.0, and 4.0 maintaining the same hydraulic diameter.

The procedure of the numerical analysis is the same as our previous study [10]; thus, the procedure is briefly explained. After applying a filtering operation to the incompressible Navier–Stokes equation with a filter width equal to the grid spacing [6], the dimensionless governing equations scaled by a length scale, l $(=0.5D)$, and a mean friction velocity, u_*, became a set of dimensionless governing equations with respect to grid resolvable components indicated by overbars as $(\bar{u},\bar{v},\bar{w})$ under the assumption of constant fluid properties. As shown in equation (1), F_i was an external force term including the Coriolis force, and the buoyancy term was ignored in this study. The mean pressure gradient term (with a value of 2) was added to the external force term as shown in the following equation:

$$F_i\begin{pmatrix}0\\ 2Ro_*\bar{w}\\ -2Ro_*\bar{v}+2\end{pmatrix}. \tag{1}$$

The temperature was made dimensionless by using the bulk temperature, T_b, and the friction temperature, T_r, as $\theta=(T-T_b)/T_r$. Accordingly, the dimensionless energy equation was derived for the grid resolvable component, $\bar{\theta}$.

Subgrid-scale components of stress, τ_{SGSij}, and energy flux, α_{SGSj}, are expressed as follows:

$$\tau_{SGSij}=2\nu_t\bar{S}_{ij} \quad \text{and} \quad \alpha_{SGSj}=\frac{\nu_t}{Pr_{SGS}}\frac{\partial\bar{\theta}}{\partial x_j}, \tag{2}$$

where

$$\bar{S}_{ij}=\frac{1}{2}\left(\frac{\partial\bar{u}_i}{\partial x_j}+\frac{\partial\bar{u}_j}{\partial x_i}\right), \tag{3}$$

$$\nu_t=C_S^2(\Delta x\Delta y\Delta z)^{2/3}\sqrt{2\bar{S}_{ij}\bar{S}_{ij}}. \tag{4}$$

In this study, the dynamic subgrid-scale model developed by Germano et al. [13] was used in order to calculate the value of C_S as a function of spatial location with the stable computational procedure of Lilly [14].

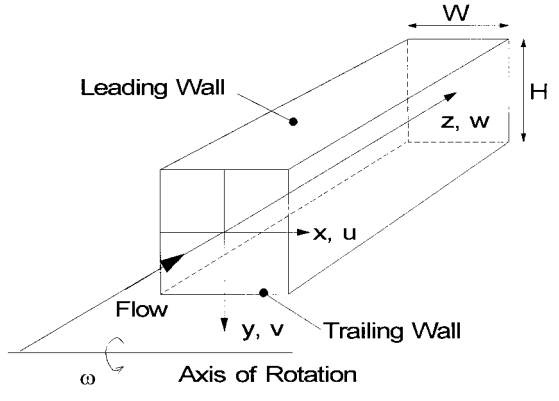

Fig. 1. Schematic of a rotating duct and coordinate system.

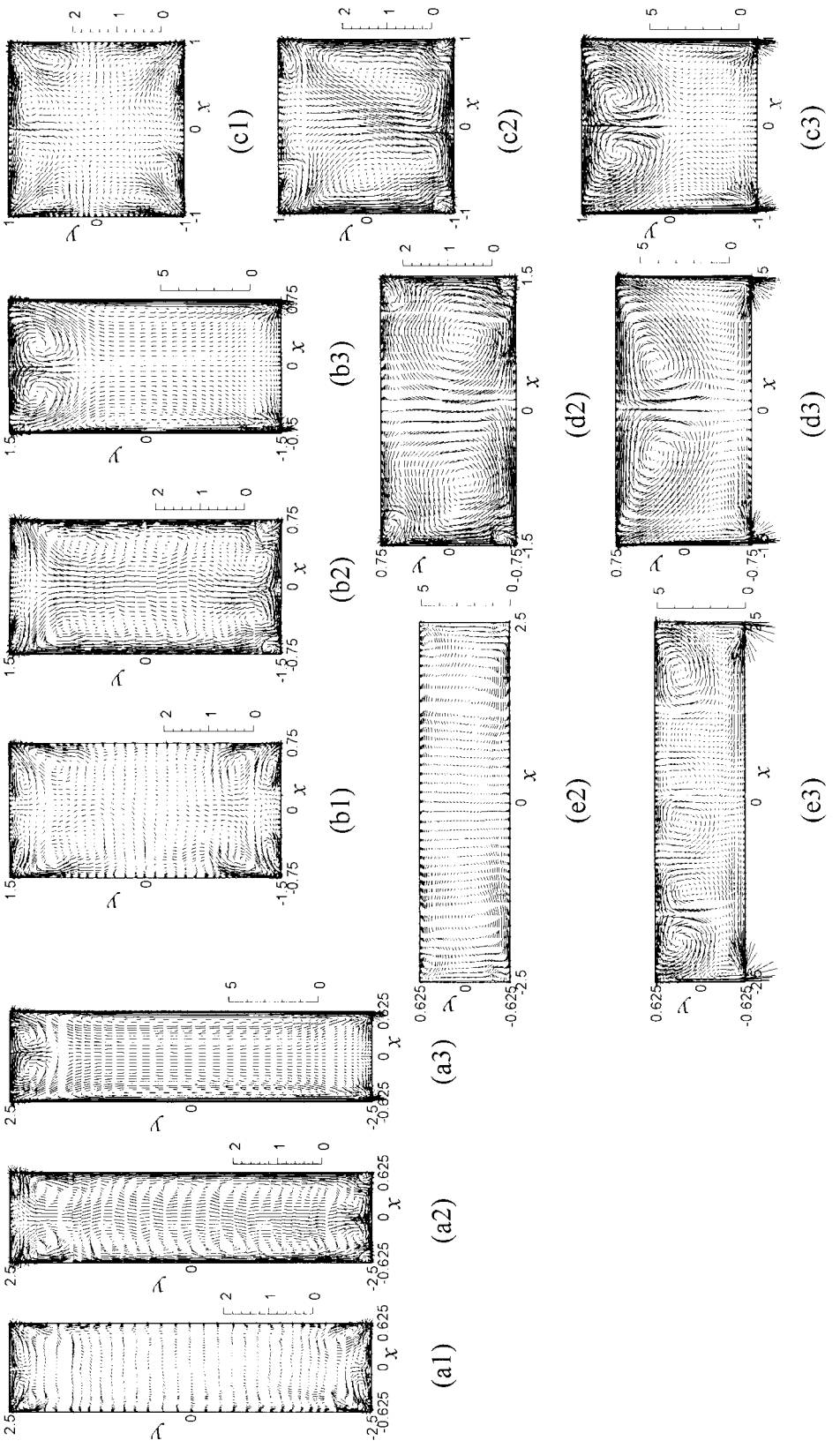

Fig. 2. Change in averaged velocity vectors of secondary flow caused by rotation ((a), (b), (c), (d), (e) correspond to aspect ratio 4.0, 2.0, 1.0, 0.5, 0.25, respectively. The numbers (e.g. (a1), (a2), (a3)) correspond to $Ro_* = 0$, 0.1, 2.0, respectively. (d1) and (e1) are not shown because those are the same as (b1) and (a1), respectively. In each figure, upper and lower walls correspond to trailing and leading walls, respectively).

The turbulent Prandtl number for the subgrid-scale component, Pr_{SGS}, was set to 0.5. The width of the test filter was double the grid spacing and the space filter was accurate to fourth order [15].

Discretization was performed by a finite difference method. The spatial and temporal discretization schemes were the fourth order central differencing method and the Crank–Nicolson method for the viscous term, and the fourth order differencing method satisfying the conservative property [16] and the second order Adams–Bashforth method for the convective term, respectively. The external force term was also treated by the second order Adams–Bashforth method. The pressure field was treated following the SMAC method [17], and the algebraic equation for each variable was solved by using the SOR method. The computational domain was $2 \times 2 \times 12$ ($A_R = 1.0$), $1.5 \times 3 \times 12$ ($A_R = 2.0$), and $1.25 \times 5 \times 12$ ($A_R = 4.0$), in x, y, and z directions, respectively. This can be expressed by using an inner length scale, ν/u_*, as $700 \times 700 \times 4200$ for the stationary square case. The variables scaled by the inner scales will be indicated by adding a superscript, $+$.

The Reynolds number, Re_* ($= u_* l/\nu$), was 350, and the rotation number, Ro_* ($= \omega l/u_*$), was varied from 0 to 5.0. The Reynolds number defined by the mean velocity and the hydraulic diameter, Re_m, was in the range of 11,000–12,000 for the stationary cases of the five different A_Rs. At the wall boundary, no-slip and constant heat flux conditions were imposed. At the inlet and outlet boundaries, the periodic boundary condition was imposed in order to obtain a fully developed flow.

The local Nusselt number, Nu_L, was calculated by using the temperature averaged both temporally and spatially in the streamwise direction considering the homogeneity of the phenomena in this direction. The averaged Nusselt number was calculated by using the integrally averaged temperature difference on the area in question.

Staggered grids in the physical domain were contracted to the walls in the x and y directions by using a tangent hyperbolic function. In the streamwise, z direction, grid points were located uniformly. This physical domain was transformed into a computational domain of uniform grid spacing. The grid number was $65 \times 65 \times 65$ for most cases, although for the cases of small aspect ratio and high rotation number ($A_R = 0.5$, $Ro_* = 5.0$ and $A_R = 0.25$, $Ro_* = 2.0$, 5.0), a grid number of $95 \times 47 \times 65$ in x, y, and z directions was used instead because of the instability seen while performing the computation. These grid configurations gave a grid spacing of Δx^+, $\Delta y^+ = 0.5$–68 and $\Delta z^+ = 65$ with 2 to 7 grid points within the viscous sublayer (x^+, $y^+ < 5$) for the stationary case within the present A_R range. In the rotating cases, the thickness of the boundary layer varied on each wall, and for the highest rotation number the trailing wall resulted in friction velocity increasing by 30%. The time step interval was $\Delta t = 5.0 \times 10^{-4}$, which can be expressed as $\Delta t^+ = 0.175$ when made dimensionless by an inner time scale, ν/u_*^2. The computation was started using the lower rotation number result as an initial condition. The calculations were carried out to 40,000 steps to fully develop the flow. After the initial 40,000 steps were performed, an additional 20,000 steps ($t = 10$ or $t^+ = 3{,}500$) were performed for computing the statistical values. This 20,000 step computation needed about 65,000 CPU seconds using an NEC SX4B.

3. Results and discussion

Fig. 2 shows the averaged velocity vectors of the secondary flow in the x–y plane. In this study, the averaged values were time-averaged and at the same time spatially averaged in the streamwise direction taking advantage of the homogeneity of the phenomena in that direction. In each figure, Fig. 2(a), (b), (c), (d), and (e) correspond to aspect ratio, A_R, of 4.0, 2.0, 1.0, 0.5, and 0.25, respectively. The numbers following the letters in the parentheses, (a1), (a2), and (a3), correspond to the rotation number, Ro_*, of 0, 0.1, and 2.0, respectively. The flow field of this study should be symmetric with respect to the plane of $x = 0$, but the results are shown without the average using this symmetric property. In Fig. 2, the results show that the symmetry was enough to verify that the sample size was sufficiently large for the statistical average. In the stationary case ((1) in each figure) of every aspect ratio case, the averaged vectors show the well-known secondary flow of Prandtl's second kind which induces the flow component directing to the four corners. When the rotation number is low ($Ro_* = 0.1$; (2) in each figure), the secondary flow induced by the Coriolis force is observed in the flow component coming from the suction (leading) surface (the lower wall in the figure) to the pressure (trailing) surface (the upper wall in the figure) at the transverse center ($x = 0$). When the rotation number is further increased ($Ro_* = 2.0$; (3) in each figure), there appears a vortex pair locating near the trailing wall and inducing the flow from the center on the trailing wall to the duct center except in the lowest aspect ratio, $A_R = 0.25$, of Fig. 2(e3), in which, on the contrary, there appears three vortex pairs in the transverse direction. When the aspect ratio is larger ($A_R \geqq 1.0$), a pair of vertically elongated vortex sticking to the side walls is formed. This pair of vortex is forced to move to the lower corner side in Fig. 2(d3) and (e3) as the aspect ratio decreases.

Figs. 3–5 show the effect of the rotation on the root-

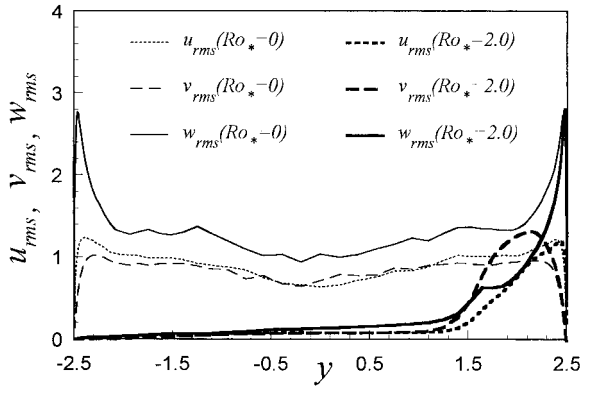

Fig. 3. Effect of rotation on turbulence intensity ($A_R=4.0$).

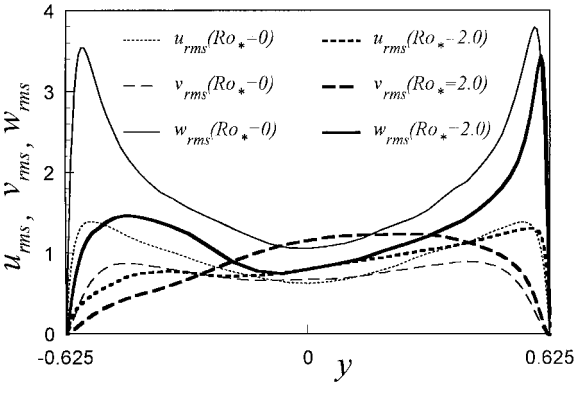

Fig. 5. Effect of rotation on turbulence intensity ($A_R=0.25$).

mean-square (rms) values of the three velocity components at the transverse center ($x=0$) for aspect ratios $A_R=4.0$, 1.0, and 0.25, respectively. In each figure, the stationary case (thin lines) shows a symmetric profile with respect to $y=0$. The rotation of the duct changes this profile to one in which the large value is only near the pressure (trailing) surface (the right boundary in the figures). On the other hand, near the suction (leading) surface (the left boundary in the figures) the rms values decay. When Figs. 3–5 are compared to one another, it is seen that a smaller aspect ratio suppresses the decay of the turbulence on the suction side. This tendency can be understood by considering the fact that the flow becomes two-dimensional as the aspect ratio decreases. The effect of the Coriolis force on the turbulent flow field can be categorized into two aspects: the direct influence on the fluctuating components and the indirect influence through the streamwise mean velocity profile changed by the Coriolis induced secondary flow [8]. The direct influence of the Coriolis force can be understood by considering additional production terms introduced by the rotation in the transport equations of the Reynolds stress; especially, source and sink terms for the wall normal component of the Reynolds normal stress near the pressure and suction surfaces, respectively [8]. It was reported that the direct influence became dominant for the aspect ratio of $A_R=1/7$ ($=0.143$) because of the two-dimensionality attained in the transversely flat rectangular duct [11]. The dominant direct influence can be understood by considering the negligibly small transverse gradient of the streamwise velocity which induces a transversely uniform Coriolis force acting in the y direction [see Eq. (1)]. This leads to the balance between the pressure gradient and the Coriolis force in the y direction for small aspect ratios. On the other hand, for larger aspect ratios, the larger transverse gradient of the streamwise velocity caused by the transversely narrow flow passage results in a stronger secondary flow due to a larger variation of the Coriolis force as compared to smaller aspect ratios. Within the present aspect ratio range, the indirect influence of the Coriolis induced secondary flow was always observed. In addition, the direct influence acting on the fluctuating components became relatively stronger for smaller aspect ratios, although the flow did not become fully two-dimensional.

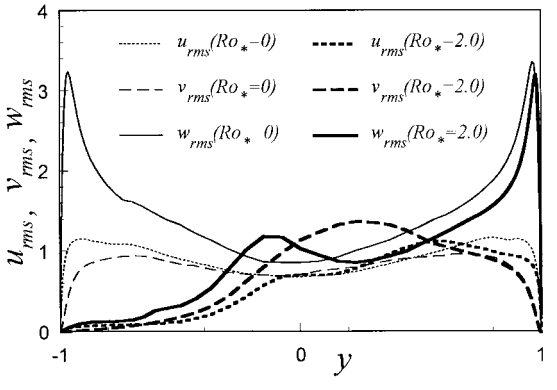

Fig. 4. Effect of rotation on turbulence intensity ($A_R=1.0$).

Figs. 6–8 show the isocontours of the averaged streamwise velocity, temperature, and turbulent kinetic energy, k, including subgrid-scale components in the x–y plane, respectively. The computational conditions of each figure is the same as those in Fig. 2. In the stationary case of (1) in each figure, each profile of averaged variables has two-dimensional variation in both x and y directions. When the rotation number is low ($Ro_*=0.1$; (2) in each figure), both velocity and temperature fields shift to the pressure (trailing) side, and the turbulent kinetic energy has larger and smaller values near the pressure and suction surfaces, respectively. When the rotation number is further increased ($Ro_*=2.0$; (3) in each figure), the flow field of Fig. 6 shows a transversely uniform profile. This uniformity

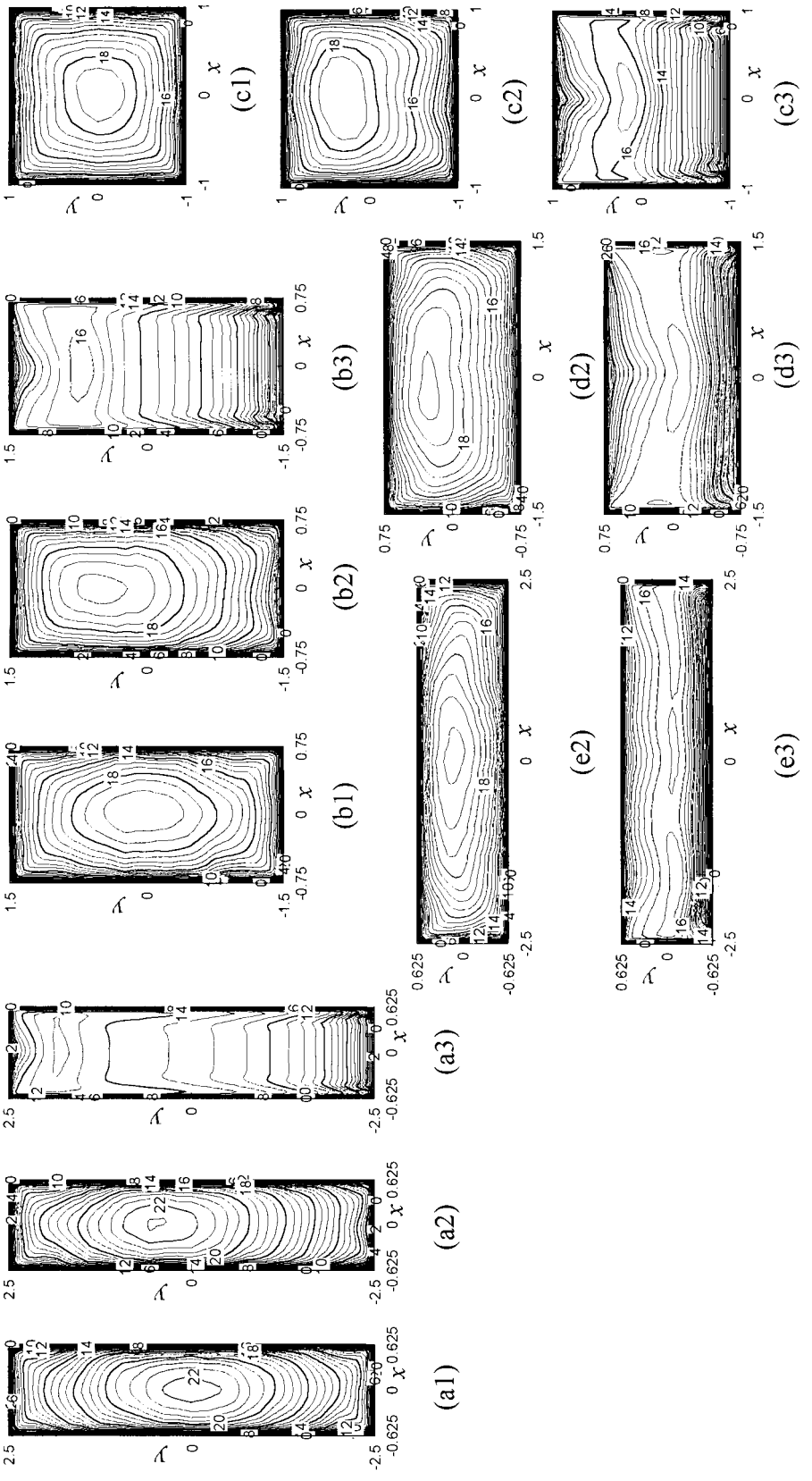

Fig. 6. Change in averaged streamwise velocity caused by rotation (legend is the same as that of Fig. 2).

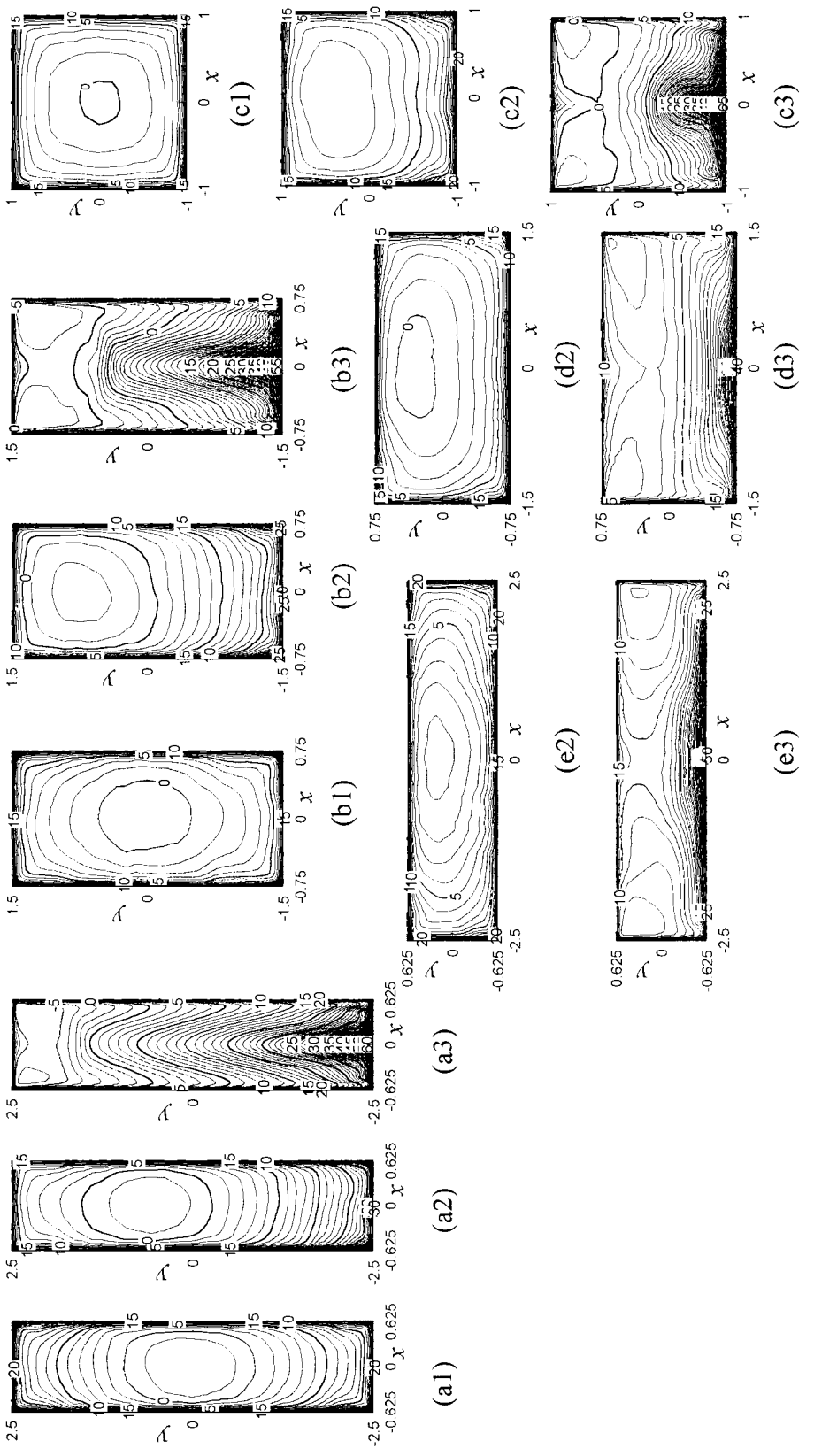

Fig. 7. Change in averaged temperature caused by rotation (legend is the same as that of Fig. 2).

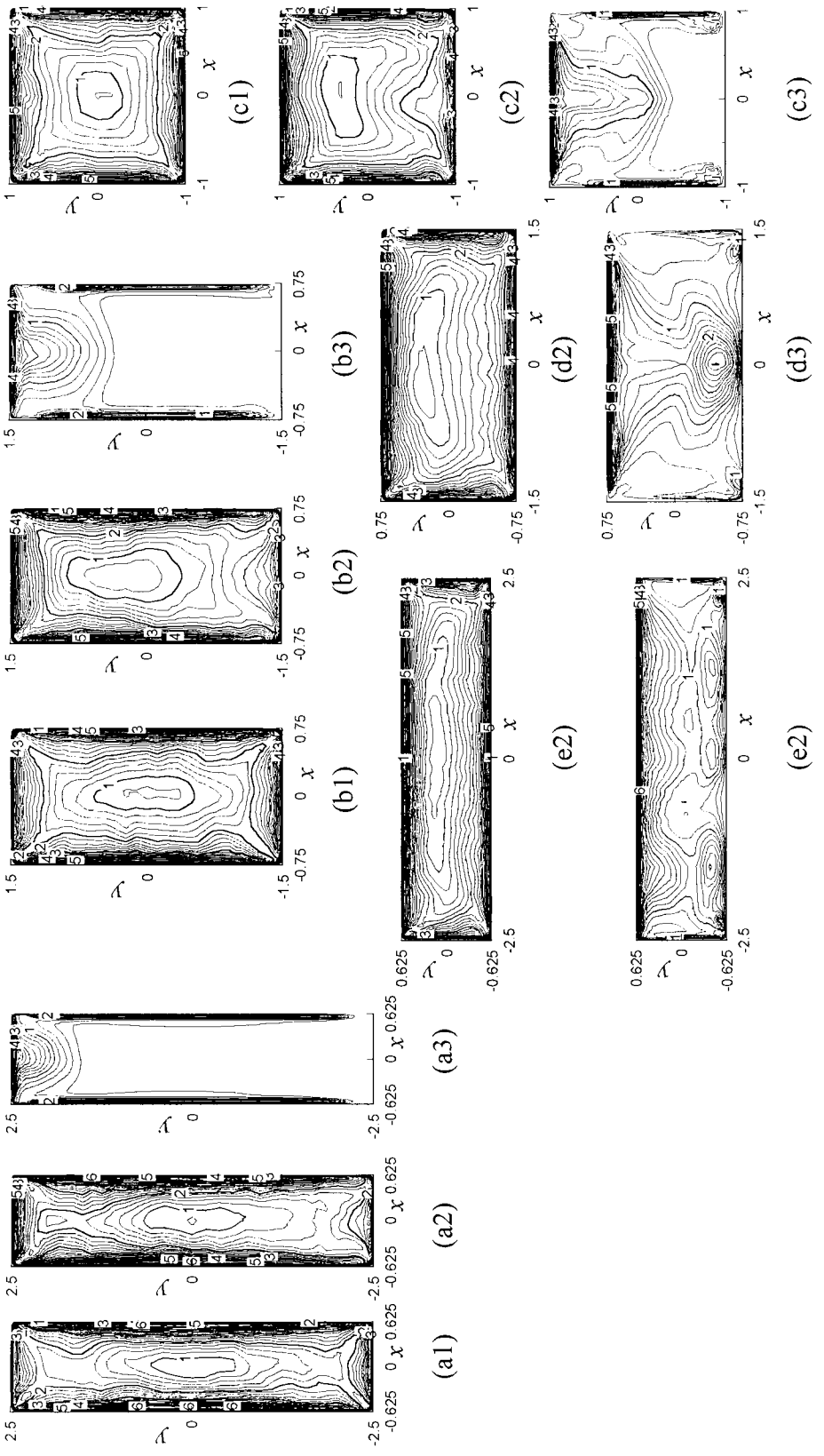

Fig. 8. Change in turbulent kinetic energy caused by rotation (legend is the same as that of Fig. 2).

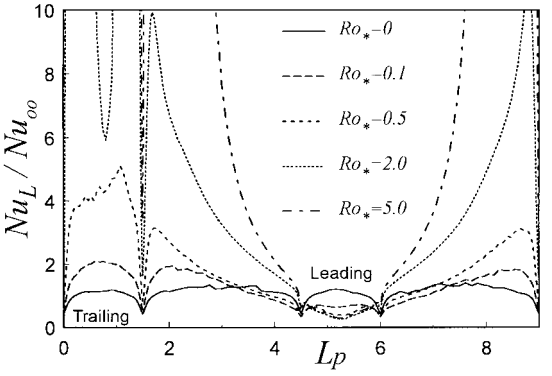

Fig. 9. Peripheral variation of local Nusselt number for various Ro_* ($A_R = 2.0$).

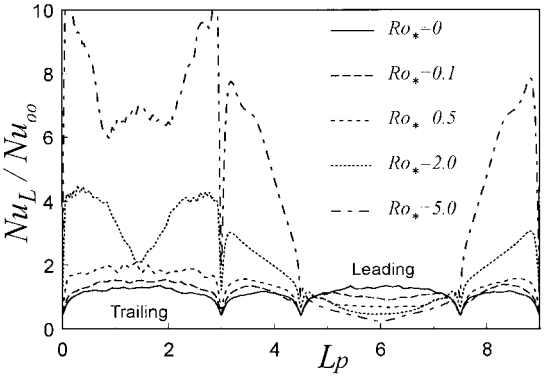

Fig. 10. Peripheral variation of local Nusselt number for various Ro_* ($A_R = 0.5$).

can be understood by considering the balance between the pressure gradient term and the Coriolis force which does not have a component in the transverse (x) direction. For this high rotation number case, especially the cases of $A_R \geq 1.0$, the temperature profile shows a projected (convex) profile at the center on the suction surface in Figs. 6(a3)–(c3); this temperature profile, dissimilar to the transversely uniform velocity profile, must be the consequence of the absence of the Coriolis force and the pressure gradient in the energy equation. For larger aspect ratios ($A_R \geqq 1.0$), the velocity boundary layer on the pressure surface becomes much thinner than that on the suction surface, and the location of maximum velocity shifts to the pressure surface. On the contrary, for smaller aspect ratios ($A_R = 0.5$ and 0.25) in Figs. 6(d3) and (e3), the location of maximum velocity shifts to the suction surface. In the former case of $A_R \geqq 1.0$, the Coriolis induced secondary flow dominates the phenomena; on the other hand, in the latter case of $A_R = 0.5$ and 0.25 the direct influence of the Coriolis force on the fluctuating velocity components must be dominant. The result of the latter case, the shift of the maximum velocity location to the suction surface, is similar to the previous result of the turbulent flow in a rotating two-dimensional channel where only the direct influence of the Coriolis force exists [8].

In Fig. 8, the turbulent kinetic energy on the suction side decays more rapidly for larger aspect ratios. This must imply that the indirect influence of the Coriolis force on the turbulence through the streamwise mean velocity profile is more intense than the direct influence within the present computational conditions.

Figs. 9 and 10 show the peripheral variation of the local Nusselt number on the four walls for $A_R = 2.0$ and 0.5, respectively, with various Ro_*. The Nusselt number is normalized using the following empirical correlation for a fully developed pipe flow (Kays and Crawford [18]):

$$Nu_\infty = 0.022 Re_m^{0.8} Pr^{0.5}. \quad (5)$$

In both figures, as the rotation number increases, the Nusselt number increases and decreases on the pressure (trailing) and suction (leading) surfaces, respectively. On the side walls, the Nusselt number decreases from the trailing side to the leading side, and the symmetric profile is observed with respect to the midpoints of both the trailing and leading walls. The larger aspect ratio case of Fig. 9 gives a higher enhancement rate on the trailing and side walls as the rotation number increases as compared to the smaller aspect ratio case of Fig. 10. On the trailing wall, the Nusselt number profile shows a concave shape at the center of the wall, which must be caused by the vortex pair locating near the trailing wall and transporting the fluid from the trailing wall to the main flow as seen in Fig. 2.

Fig. 11 shows the effect of rotation on the wall-averaged Nusselt number, Nu_w. In the figure, the horizon-

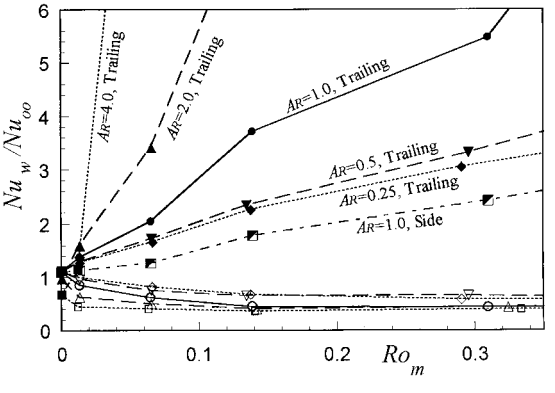

Fig. 11. Effect of rotation on heat transfer averaged for each wall (for the aspect ratio, A_R, ■□:4.0, ▲△:2.0, ●○:1.0, ▼▽:0.5, ◆◇:0.25; filled and open symbols are for trailing and leading walls, respectively, except for ◩: side wall of $A_R = 1.0$).

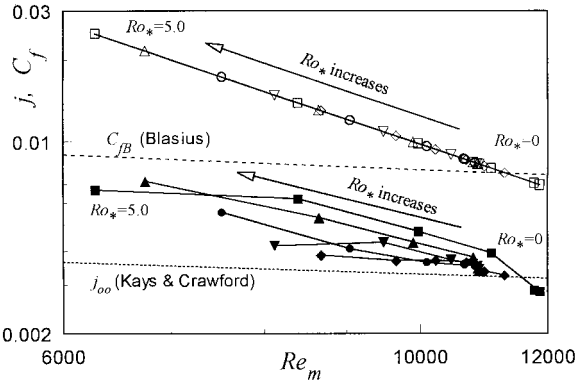

Fig. 12. Effect of rotation on C_f and j (for the aspect ratio, A_R, ■□: 4.0, ▲△: 2.0, ●○: 1.0, ▼▽: 0.5, ◆◇: 0.25; filled and open symbols are for j and C_f, respectively).

tal axis is the rotation number, Ro_m, defined by using the mean velocity and the hydraulic diameter. Because it is widely used in experiments, this definition was adopted to allow for easier future reference by other researchers. As Ro_m increases, Nu_w increases and decreases on the pressure (trailing) and suction (leading) surfaces, respectively. In addition, the increase in the aspect ratio drastically enhances the heat transfer on the pressure surface, although on the suction surface it mildly suppresses the heat transfer. The value of the side wall for $A_R = 1.0$, shown in the figure for comparison, shows mild enhancement as Ro_m increases. It should be noted that the Re_m decreases as Ro_m increases because the increase of Ro_m induces the increase of pressure loss and thus the decrease of flow rate in the present computation.

Fig. 12 shows the friction coefficient, C_f, and the Colburn's j factor. In the stationary case which is displayed by the right most plot for each symbol, both C_f and j approximately agree with the empirical correlations of Kays and Crawford [Eq. (5)] and Blasius [Eq. (6)]:

$$C_{fB} = 0.079 Re_m^{-0.25}. \quad (6)$$

When Ro_* increases, the mean streamwise velocity decreases (the data move to left hand side in the figure), and both C_f and j increase. When the aspect ratio is varied, the friction coefficient is well correlated on a line in the figure; on the contrary, the Colburn's j factor gives higher values for larger aspect ratios, although a few exceptions are seen at higher rotation numbers. As seen in Figs. 9 and 10, the flow field variation induced by the larger aspect ratio enhances the heat transfer on the trailing and side walls more intensely than that in the smaller aspect ratio cases, and therefore the duct-averaged heat transfer has a higher value for larger aspect ratios.

4. Conclusions

Within the aspect ratio range ($A_R = 0.25$–4.0) examined in this study, the effect of the Coriolis force on the turbulent flow in the orthogonally rotating duct was seen in both the indirect and direct influences which were caused by the mean velocity profile modified by the Coriolis induced secondary flow and by the direct action of the Coriolis force on the fluctuating components, respectively. The relative contribution ratio of these two influences changed according to the value of the aspect ratio. The increase in the rotation number caused the increase and decrease of the heat transfer on the pressure and suction surfaces, respectively. The duct-averaged values, the friction coefficient and the Colburn's j factor, increased as compared to the empirical correlations for the fully developed flow. The Colburn's j factor showed larger values for larger aspect ratios, which were caused by the more intense heat transfer enhancement on the pressure (trailing) surface and the side walls as compared to that of the smaller aspect ratio cases.

References

[1] B. Lakshminarayana, Fluid Dynamics and Heat Transfer of Turbomachinery, Wiley, New York, 1996 Chap. 7.
[2] S.V. Ekkad, J.C. Han, Detailed heat transfer distributions in two-pass square channels with rib turbulators, Int. J. Heat Mass Transf. 40-11 (1997) 2525–2537.
[3] T. Bo, H. Iacovides, B.E. Launder, Developing buoyancy-modified turbulent flow in ducts rotating in orthogonal mode, Trans. ASME, J. of Turbomachinery 117 (1995) 474–484.
[4] A. Huser, S. Biringen, Direct numerical simulation of turbulent flow in a square duct, J. Fluid Mech. 257 (1993) 65–95.
[5] S. Gavrilakis, Numerical simulation of low Reynolds number turbulent flow through a straight square duct, J. Fluid Mech. 244 (1992) 101–129.
[6] R.K. Madabhushi, S.P. Vanka, Large eddy simulation of turbulence-driven secondary flow in a square duct, Phys. Fluids A3-11 (1991) 2734–2745.
[7] T. Kajishima, Y. Miyake, T. Nishimoto, Large eddy simulation of turbulent flow in a square duct, Trans. JSME(B) 57-540 (1991) 2530–2537 (in Japanese).
[8] B.E. Launder, D.P. Tselepidakis, B.A. Younis, A second-moment closure study of rotating channel flow, J. Fluid Mech. 183 (1987) 63–75.
[9] A. Murata, S. Mochizuki, T. Takahashi, Local heat transfer measurements of an orthogonally rotating square duct with angled rib turbulators, Int. J. Heat Mass Transf. (in press).
[10] A. Murata, S. Mochizuki, Large eddy simulation with a dynamic subgrid-scale model of turbulent heat transfer in an orthogonally rotating smooth square duct, Int. J. Heat Mass Transf., submitted.

[11] B.A. Younis, Prediction of turbulent flows in rotating rectangular ducts, Trans. ASME, J. of Fluids Eng. 115 (1993) 646–652.
[12] S. Dutta, M.J. Andrews, J.C. Han, Prediction of turbulent flow and heat transfer in rotating square and rectangular smooth channels, ASME Paper, 96-GT-234 (1996).
[13] M. Germano, U. Piomelli, P. Moin, W.H. Cabot, A dynamic subgrid-scale eddy viscosity model, Phys. Fluids A3-7 (1991) 1760–1765.
[14] D.K. Lilly, A proposed modification of the Germano subgrid-scale closure method, Phys. Fluids A4-3 (1992) 633–635.
[15] H. Miyata, Analysis of Turbulent Flows, Computational Fluid Dynamics Series 3, p. 97, University of Tokyo Press, Tokyo (1995) (in Japanese).
[16] Y. Morinishi, Conservative properties of finite difference schemes for incompressible flow (2nd report, schemes in staggered and collocated grid systems), Trans. JSME(B) 62-604 (1996) 4098–4105 (in Japanese).
[17] A.A. Amsden, F.H. Harlow, A simplified MAC technique for incompressible fluid flow calculations, J. of Comp. Phys 6 (1970) 322–325.
[18] W.M. Kays, M.E. Crawford, Convective Heat and Mass Transfer, 3rd ed. McGraw-Hill, New York, 1993.